nature astronomy

LETTERS

https://doi.org/10.1038/s41550-021-01491-0

Check for updates

A snapshot of the oldest active galactic nuclei feedback phases

M. Brienza[1,2]✉, T. W. Shimwell[3,4], F. de Gasperin[2,5], I. Bikmaev[6,7], A. Bonafede[1,2,5], A. Botteon[4], M. Brüggen[5], G. Brunetti[2], R. Burenin[8], A. Capetti[9], E. Churazov[8,10], M. J. Hardcastle[11], I. Khabibullin[8,10], N. Lyskova[8], H. J. A. Röttgering[4], R. Sunyaev[8,10], R. J. van Weeren[4], F. Gastaldello[12], S. Mandal[4], S. J. D. Purser[13], A. Simionescu[4,14,15] and C. Tasse[16,17,18]

Active galactic nuclei inject large amounts of energy into their host galaxies and surrounding environment, shaping their properties and evolution[1,2]. In particular, active-galactic-nuclei jets inflate cosmic-ray lobes, which can rise buoyantly as light 'bubbles' in the surrounding medium[3], displacing and heating the encountered thermal gas and thus halting its spontaneous cooling. These bubbles have been identified in a wide range of systems[4,5]. However, due to the short synchrotron lifetime of electrons, the most advanced phases of their evolution have remained observationally unconstrained, preventing us from fully understand their coupling with the external medium, and thus active galactic nuclei feedback. Simple subsonic hydrodynamic models[6,7] predict that the pressure gradients, naturally present around the buoyantly rising bubbles, transform them into toroidal structures, resembling mushroom clouds in a stratified atmosphere. The way and timescales on which these tori will eventually disrupt depend on various factors including magnetic fields and plasma viscosity[8,9]. Here we report observations below 200 MHz, sensitive to the oldest radio-emitting particles, showing the late evolution of multiple generations of cosmic-ray active-galactic-nuclei bubbles in a galaxy group with unprecedented level of detail. The bubbles' buoyancy power can efficiently offset the radiative cooling of the intragroup medium. However, the bubbles still have not thoroughly mixed with the thermal gas, after hundreds of million years, probably under the action of magnetic fields.

The galaxy group is named 'Nest200047' and was first identified by ref. [10] (more details in Supplementary Information). At its centre lies the massive elliptical galaxy MCG+05-10-007, with spectroscopic redshift $z = 0.01795 \pm 0.00015$ (ref. [11]) (Supplementary Fig. 2). We first discovered the system in the radio band through the Low Frequency Array (LOFAR)[12] Two-Meter Sky Survey (LoTSS)[13] at 144 MHz thanks to the bizarre morphology of its radio emission (Fig. 1 and Supplementary Fig. 1). It was then further investigated using follow-up LOFAR observations at 53 MHz and X-ray observations performed with the extended Roentgen Survey with an Imaging Telescope Array (eROSITA)[14] onboard the Spectrum–Roentgen–Gamma (SRG) mission (R.S. et al., manuscript in preparation). The X-ray emission from the group in the 0.5–2 keV band was clearly detected for the first time by eROSITA (Fig. 2 and Supplementary Fig. 3) and appears to be nicely centred at the position of MCG+05-10-007. We estimated that the temperature of the intragroup medium (IGrM) is $kT_X \approx 2 \pm 0.5$ keV and its luminosity is $L_X = 5 - 10 \times 10^{42}\,\mathrm{erg\,s^{-1}}$. The total mass of the system lies in the range $M_{500} = 3 - 7 \times 10^{13}\,M_{\odot}$, placing Nest200047 among typical groups of galaxies, consistent with the initial classification[10].

Our new LOFAR images at 53 MHz and 144 MHz reveal that the galaxy group is permeated by non-thermal plasma with complex morphology extending up to ~200 kpc from the centre. In particular, the central galaxy shows active galactic nuclei (AGN) activity in the form of two nearly symmetric radio jets about 25 kpc long. These jets have a radio luminosity equal to $L_{144\,\mathrm{MHz}} = 1.7 \times 10^{23}\,\mathrm{W\,Hz^{-1}}$ (marked as A in Fig. 1, top panels) and a spectral index typical for freshly injected plasma ($\alpha^{144\ \mathrm{MHz}}_{53\ \mathrm{MHz}}(\mathrm{A}) \approx 0.6 \pm 0.18$, $S \propto \nu^{-\alpha}$, where S is the flux density and ν is the frequency, Fig. 3). As shown in Fig. 1, top-right panel, in the innermost regions of the jets we observe two symmetric, very compact components, suggesting that the AGN is recurrently inflating new bubbles of radio-emitting plasma. This scenario is also supported by the presence of two extra pairs of low-surface-brightness lobes located beyond the inner jets (marked as B and C in Fig. 1, top panels). These can be interpreted as remnant lobes of past AGN-jet outbursts[15], or as a series of bubbles of plasma, which regularly detach from a continuously operating jet. The spectral-index gradient observed in these three pairs of lobes ($\alpha^{144\ \mathrm{MHz}}_{53\ \mathrm{MHz}}(\mathrm{B}) \approx 0.8 \pm 0.18$ and $\alpha^{144\ \mathrm{MHz}}_{53\ \mathrm{MHz}}(\mathrm{C}) \approx 1.2 \pm 0.18$) is consistent with electrons being older at larger distances from the central AGN. At a distance of about 200 kpc from the centre of the galaxy group, we detect a complex array of filamentary radio-emitting structures connected to the AGN lobes C1 and C2 by bridges of radio emission. These filaments are oriented in various directions and often show sharp bends and double strands of very narrow emission. Particularly striking are the 'box-shaped' filament in the

[1]Dipartimento di Fisica e Astronomia, Università di Bologna, Bologna, Italy. [2]INAF - Istituto di Radio Astronomia, Bologna, Italy. [3]ASTRON, Netherlands Institute for Radio Astronomy, Dwingeloo, the Netherlands. [4]Leiden Observatory, Leiden University, Leiden, the Netherlands. [5]Hamburger Sternwarte, Universität Hamburg, Hamburg, Germany. [6]Department of Astronomy and Satellite Geodesy, Kazan Federal University, Kazan, Russia. [7]Academy of Sciences of Tatarstan, Kazan, Russia. [8]Space Research Institute (IKI), Russian Academy of Sciences, Moscow, Russia. [9]INAF - Osservatorio Astrofisico di Torino, Pino Torinese, Italy. [10]Max Planck Institute for Astrophysics, Garching bei München, Germany. [11]Centre for Astrophysics Research, University of Hertfordshire, College Lane, UK. [12]INAF- Istituto di Astrofisica Spaziale e Fisica Cosmica (IASF) - Milano, Milan, Italy. [13]Astronomy & Astrophysics Section, Dublin Institute for Advanced Studies, Dublin, Ireland. [14]SRON Netherlands Institute for Space Research, Utrecht, the Netherlands. [15]Kavli Institute for the Physics and Mathematics of the Universe (WPI), The University of Tokyo, Kashiwa, Japan. [16]GEPI, Observatoire de Paris, CNRS, Université Paris Diderot, 5 place Jules Janssen, Meudon, France. [17]USN, Observatoire de Paris, CNRS, PSL, UO, Nançay, France. [18]Centre for Radio Astronomy Techniques and Technologies, Department of Physics and Electronics, Rhodes University, Grahamstown, South Africa. ✉e-mail: m.brienza@ira.inaf.it

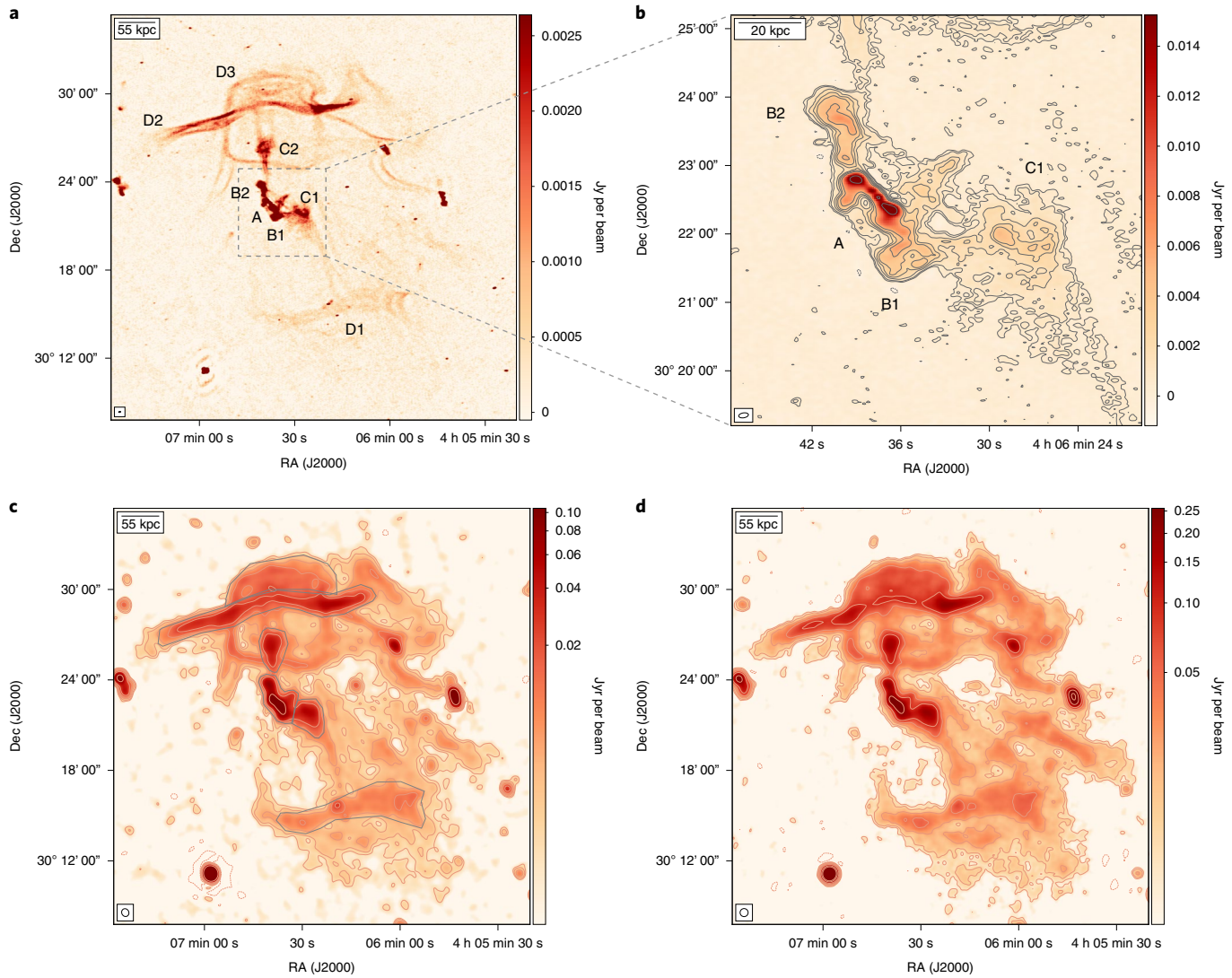

Fig. 1 | LOFAR images showing the complex non-thermal radio emission in the galaxy group Nest200047. a, LOFAR image at 144 MHz with resolution of 4.3 × 8.6 arcsec and noise of $\sigma = 0.166$ mJy per beam. Letters mark the most relevant morphological features as described in the text. **b**, Zoom-in on the central AGN at 144 MHz and resolution of 4.3 × 8.6 arcsec. Contours are drawn at −3, 3, 5, 10, 15, 20, 30 and 100 × σ. **c**, LOFAR image at 144 MHz with resolution of 28.3 × 30.5 arcsec and noise of $\sigma = 0.57$ mJy per beam. Contours are drawn at −3, 3, 5, 10, 20, 40, 100 and 180 × σ. **d**, LOFAR image at 53 MHz with resolution of 32 arcsec and noise of $\sigma = 2.3$ mJy per beam. Contours are drawn at −3, 3, 5, 10, 20, 40, 100 and 180 × σ. The beam size of each map is shown in the bottom-left corner of each panel.

north and the main filament (D2), which extends in the east–west direction for ~350 kpc and has a width of a few kiloparsecs, proving the presence of magnetic field coherence on very large scales. A similar elongated structure is present in the south too, although much fainter and with less defined morphology (marked as D1). Moreover, the LOFAR images at 25 arcsec resolution reveal the presence of diffuse extended emission embedding the filaments, with increasing radio spectral indices (up to $\alpha_{53\,\mathrm{MHz}}^{144\,\mathrm{MHz}} \approx 2.5 \pm 0.3$), that is, older emission, towards the source periphery.

The presence of multiple generations of AGN lobes and their clear morphological connection with the filamentary structures on larger scales, together with some tentative signs of an X-ray/radio anticorrelation on scales ~100 kpc, suggest that the recurrent AGN-jet activity is responsible for the creation of the entire observed emission in Nest200047. The edge-brightened rim partly filled with radio-emitting plasma observed in the X-ray image (Fig. 2) strongly resembles other AGN feedback-driven objects, such as M84 (ref. [16]). In particular, the morphology of the non-thermal plasma in the northern region of the group has a strong resemblance with the 'mushroom-shaped' structure observed in M87 (refs. [17,18]), as well as with X-ray cavities in their late phases of evolution as predicted by hydrodynamical simulations (for example, ref. [19]). Based on this, we interpret the radio-bright structures D2 and D3 as tori of plasma (that is, vortex rings) expanding in the IGrM as seen approximately edge-on and caught at a much more advanced stage of evolution with respect to M87. The spectral index in the ring D2, reaching values as flat as $\alpha_{53\,\mathrm{MHz}}^{144\,\mathrm{MHz}} \approx 0.75 \pm 0.2$, might also suggest that a mild compression of the plasma in this region is occurring, for example, as a result of a weak shock launched by a subsequent AGN outburst or of the group dynamics. The effect of this compression would indeed be to increase the synchrotron spectral break frequency by a factor of ~2.5 (ref. [20]), moving it above the currently observed frequency range. Moreover, this might contribute to shaping the morphology of the large-scale emission and to creating the observed filaments, rings and eddies[21]. We note that the morphology of D1 and D2 are reminiscent of radio relics in galaxy clusters[22].

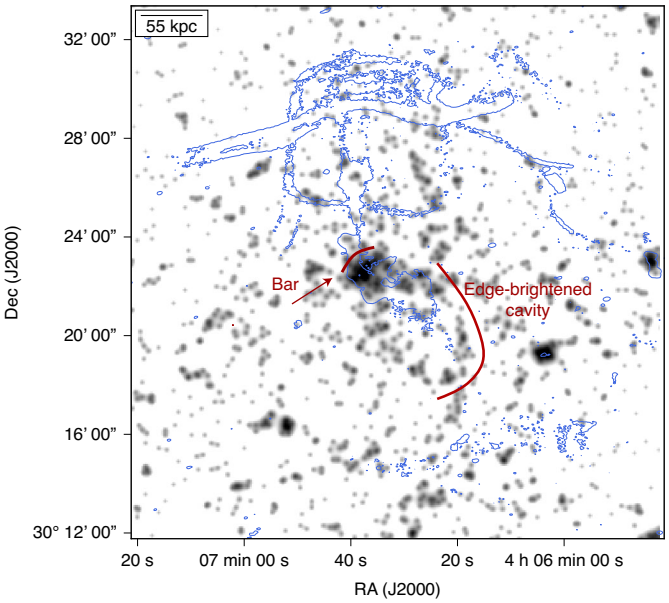

Fig. 2 | Lightly smoothed 0.5–2.3 keV eROSITA X-ray image of the galaxy group Nest200047 showing the fine X-ray substructure in the core of the group. The shape of the smoothing kernel corresponds to the point spread function (PSF) of the telescope (30 arcsec half-power diameter). Overlaid in blue is the 3σ radio contour of the LOFAR 144-MHz map at a resolution of 4.3 × 8.6 arcsec (as shown in Fig. 1). In the core of the galaxy group (central 1 arcmin), an X-ray bright bar is seen, which is orthogonal to the orientation of the inner radio jets (red arrow). On slightly larger scales (~5 arcmin), to the southwest of the nucleus, a limb-brightened X-ray cavity is present (red line), which is partly filled with the radio lobe C1. The inner 100-kpc region is qualitatively similar to other AGN feedback-driven objects, such as, for example, M84 in the Virgo cluster (for example, ref. [16]).

However, the optical (Supplementary Section 1) and X-ray data (see the 'SRG/eROSITA observations, data reduction and images' and 'X-ray surface-brightness profile, luminosity and mass' sections in the Methods) from the system do not support the presence of an ongoing major merger. Furthermore, their spectral-index distribution differs from classical relics[22] and their luminosity falls above the classical correlations found for relics[23], implying an implausibly high particle acceleration efficiency. All this makes the AGN scenario more likely.

Guided by other systems with cavities, we assume that the bubbles C2 and D3 were initially formed close to the central AGN and are now rising buoyantly, that is, subsonically, in the IGrM. The estimated buoyancy ages for these two structures are $t_{\rm buoy,C2} \gtrsim 170$ Myr and $t_{\rm buoy,D3} \gtrsim 350$ Myr. These are consistent with age estimates based on pure particle radiative losses equal to $t_{\rm rad,C2} < 350$ Myr, $t_{\rm rad,D3} < 400$ Myr or shorter if adiabatic losses are also taken into account. Such high ages have only been found in the Hydra cluster so far[24], and are about a factor 10 above the mean cavity ages found in galaxy clusters and groups[25].

Using the buoyancy timescales, we estimated the mechanical power deposited into the thermal gas by the bubbles C2 and D3 to be equal to $P_{\rm bubble,D3} = 1–4 \times 10^{42}$ erg s^{-1} and $P_{\rm bubble,C2} = 3 \times 10^{4}–1 \times 10^{42}$ erg s^{-1}. The power of the bubble D3 is compatible with the observed X-ray luminosity, implying that it might be effective at counterbalancing the IGrM cooling. The lower power of the bubble C2 suggests instead that not all AGN outbursts may have the same energetic impact on the system.

A comparison between the thermal pressure of the IGrM as derived from the X-ray emission (from $p_{\rm th} \approx 2–4 \times 10^{-12}$ dyn cm^{-2} in the core, down to ~10^{-12} dyn cm^{-2} near structures D2 and D3) and the non-thermal pressure of the radio-emitting plasma as derived from the minimum energy conditions assuming an electron/positron composition, ($p_{\rm nth} \approx 4 \times 10^{-13}$ dyn cm^{-2} in the core, down to ~2×10^{-13} dyn cm^{-2} in D2 and D3), suggests that a non-negligible energetic contribution from non-radiating protons in these structures might be present. However, such contribution cannot exceed that of radio-emitting electrons by a factor larger than ~10 if the structures are in pressure balance.

From hydrodynamic numerical simulations we know that, for a given environment, perfect vortex rings can travel much larger distances with respect to amorphous structures, which tend instead to get shredded after crossing a distance comparable with their size[26]. We suggest therefore that the observed diffuse emission might be interpreted as the leftover of disrupted bubbles, possibly combined with some level of turbulence, probably injected in the ambient medium by the AGN itself. The radio filaments show major distortions on 100 kpc scales. This might probe shear motions in the IGrM, which eventually cascade into turbulence. Under this assumption, we estimate that the energy flux dissipated by the turbulence into IGrM heat is ~4×10^{41} g s^{-3}. This suggests that a fraction between 1/10 and 1/3 of the bubble pV work (where p is the bubble pressure and V is the volume) is converted into IGrM turbulence, consistent also with turbulence dissipation fractions in merging galaxy clusters[27]. The presence of many thin two-filament structures throughout the system is also consistent with a partially turbulent medium. Indeed, on small scales, magnetohydrodynamic (MHD) turbulence can form a complex network of filamentary structures in field and density fluctuations, which are characterized by dissipative sheet-like structures with magnetic field lines along the long axis confining transverse, tangential shear layers[28]. At these scales, the anisotropic mixing naturally leads to the formation of density filaments along the field lines[29].

However, the fact that the bubbles and filaments have managed to maintain their integrity over a travelled distance of 100–200 kpc and timescales of hundreds of Myr might challenge the presence of a turbulent IGrM. One could expect indeed that the observed

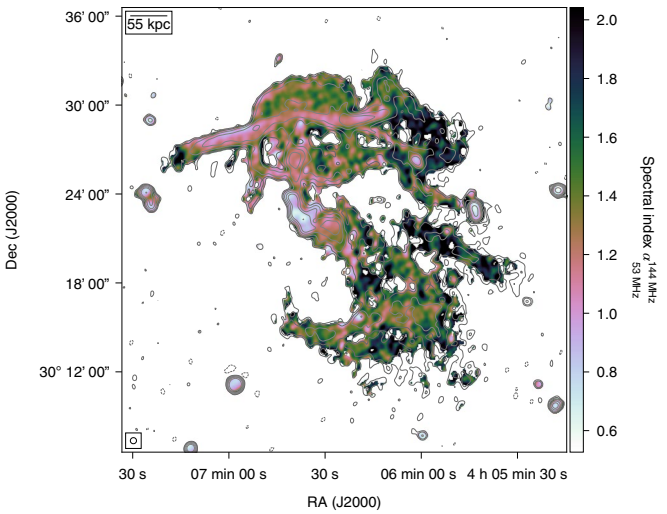

Fig. 3 | Spectral-index map in the range 53–144 MHz of the galaxy group Nest200047. The image shows an increasing spectral steepening of the non-thermal plasma towards the system peripheries, implying increasing radiative ages. The map is produced using LOFAR images with uniform weighting scheme, a Gaussian uv-taper of 25 arcsec and a restoring beam of 25 arcsec. Only pixels with surface brightness above 3σ in both maps have been used. Contour levels represent the emission at 53 MHz and are drawn at -3, 3, 5, 10, 20, 35 and 100 × σ levels, with σ = 2.7 mJy per beam. The beam size is shown in the bottom-left corner of the image.

narrow filaments (width $h \approx 2$–10 kpc) should have been destroyed by random, turbulent motions if their (one-dimensional) velocities v_h at scale $\sim h$ were much larger than $h/t_{\rm buoy} \approx 10$–$20\,{\rm km\,s^{-1}}$. For comparison, three-dimensional velocities of $\sim 50\,{\rm km\,s^{-1}}$ on scales of ~ 10 kpc would be needed to balance cooling by turbulent dissipation[30]. However, we note that thin filaments can survive in turbulent environments due to the Reynolds stress of magnetic fields that make MHD turbulence anisotropic. The physical scale at which the magnetic tension starts to play a role in turbulent dynamics is the Alfven scale, which we estimate for this system to be in the range $l_{\rm A} = 1$–5 kpc, consistent with the width of the filaments. This suggests that magnetic fields might be playing a major role in the stability of the tori/bubbles observed in Nest200047, as also proposed by simulations of magnetized vortex rings[26,31].

Nest200047 clearly offers a rare opportunity to study the evolution of AGN bubbles in a galaxy group over hundreds of millions of years, from the 'inception' of the youngest pair of lobes all the way to the break-up of the oldest generation of bubbles into the IGrM. Interestingly, despite a long and apparently rather complicated evolution, even the oldest radio plasma is not yet thoroughly mixed with the thermal plasma, neither by diffusion nor by small-scale mixing. However, this lack of mixing by no means reduces the efficiency of the AGN feedback, since the energy exchange between the bubbles and the IGrM can proceed without a thermal coupling of these phases. Thanks to its unprecedented level of detail, Nest200047 represents a unique piece of evidence for AGN-feedback models and can provide new empirical constraints to magneto–hydrodynamical simulations investigating the coupling between AGN cosmic-ray bubbles and IGrM.

Methods

LOFAR observations, data reduction and radio images. The galaxy group Nest200047 was observed with the LOFAR high-band antennas (HBA) with a central frequency of 144 MHz for a total of 16 hours. The observations were performed as part of the LoTSS[13] and pointed in the direction of the two grid pointings P061+29 and P060+31. These have a field of view with full-width at half-maximum (FWHM) of 3.96° at 144 MHz (ref. [12]) and their centres lie at 1.44 and 1.32 degrees away from the target position, respectively. The observation setup followed the standard LoTSS strategy, whose main details are summarized in Supplementary Table 1. The data were first flagged for radio frequency interference (RFI) and averaged by a factor of four in frequency by the observatory before being ingested into the LOFAR long-term archive. The archived data were then corrected for direction-independent effects such as ionospheric Faraday rotation, phase offset between stations correlations (with polarizations XX and YY) and clock offsets (see ref. [32]) using the PreFactor pipeline (for more details see: https://github.com/lofar-astron/prefactor) as described by refs. [33,34]. To correct for ionospheric distortions and errors in the beam model, a direction-dependent self-calibration was then performed using direction-dependent facet (DDF)-pipeline (for more details see: https://github.com/mhardcastle/ddf-pipeline). This pipeline is described by refs. [13,35] and uses KillMS[36,37] to derive direction-dependent calibration solutions, which are then applied during imaging with DDFacet[38]. Finally, to refine the calibration of the ionosphere and beam in the direction of the target and to allow for quicker re-imaging, we made use of the post-processing procedure described in ref. [39]. Following this, we subtracted from the visibilities all sources outside a box with sides of 0.5° centred on the target and performed a final direction-independent self-calibration of the data. The final high-resolution image was produced with WSClean (version 2.7)[40] using a Briggs weighting scheme with robust equal to −0.5. Baselines shorter than 40λ (where λ is the observation wavelength) were excluded to discard very large-scale emission ($\gtrsim$1.5°), which is unrelated to the target and typically affected by severe RFI and poorly calibrated. The final image has a resolution of 4.3 × 8.6 arcsec and a root mean squared (rms) noise of 0.166 mJy per beam (Fig. 1, top panels). To enhance the large-scale diffuse emission of the target, the data were also imaged at lower resolution, using a Briggs weighting scheme with robust equal to −0.5 and a Gaussian uv-taper of 25 arcsec. The final image has a resolution of 28.5 × 32 arcsec and rms of 0.57 mJy per beam (Fig. 1, bottom-left panel).

The target was observed with LOFAR using the low-band antennas, as part of a director's discretionary time proposal. We observed for eight hours in the frequency range 30–78 MHz with one beam pointed at the calibrator 3C196 and one on the target field. The data were taken at 1 s integration time and at frequency resolution of 64 channels per sub band, 0.196 MHz. A summary of the observation setup can be found in Supplementary Table 1. Data affected by RFI were flagged using AOflagger[41] and subsequently averaged to the time resolution of 2 s and the frequency resolution of 0.049 MHz. The calibrator data were reduced following ref. [32]. This procedure isolated some systematic effects (polarization alignment, the bandpass and the clock drifts), which we transferred to the target data. For the initial direction-independent calibration of the target field we followed ref. [42]. This procedure removes three systematic effects, averaging them across the entire field of view: the ionospheric delay, the Faraday rotation and the corrections on the beam variation with time and frequency on top of the LOFAR beam model. The result of this process is a direction-independent calibrated image that reached 3 mJy per beam in rms noise at the resolution of 45 arcsec. Due to direction-dependent errors, largely driven by ionospheric corruption[43,44], this image shows numerous artefacts, especially around bright sources, that compromise its fidelity. To correct these errors, we performed a direction-dependent calibration. The procedure followed the idea outlined in ref. [33], where a series of local 'direction-dependent' calibrators is located across the field of view. We isolated seven bright calibrators, including the target source. For each of these sources we did several cycles of phase-only self-calibration. The bright calibrators are finally subtracted from the data accounting for the effect of the ionosphere in their direction. The target direction was processed last and a few cycles of slow-amplitude corrections were also performed. As for the higher-frequency data, we imaged the data with WSClean (version 2.7)[40] using a Briggs weighting scheme with robust equal to −0.5, an inner uv-cut at 40λ and a restoring beam of 32 arcsec. The image rms noise is 2.7 mJy per beam (Fig. 1, bottom-right panel).

The flux scale of both images was checked using the brightest sources in the field as a reference. The flux densities of these sources from all publicly available surveys were used to extrapolate the expected flux densities at the frequencies of interest and these were compared with the measured values. Following this procedure, we did not find any systematic offset in the flux scale of either of the two images.

Radio-flux densities and spectral indices. To measure the radio-flux density of the source and to investigate its spectral behaviour, we have re-imaged both the 53 MHz and 144 Hz datasets using a common inner uv-cut at 40λ, uniform weighting scheme and a Gaussian uv-taper of 25 arcsec. The total flux density of the source (measured using the 3σ contours as a reference) and the flux densities of the major features within the source (measured using the regions drawn in Fig. 1, bottom-left panel) at both frequencies are listed in Supplementary Table 2, together with their respective luminosities and global spectral indices. The total errors on the flux densities were computed by combining in quadrature the flux-scale errors (10% at 53 MHz (ref. [45]) and 15% at 144 MHz (ref. [13])) and the image noise multiplied by the flux-density integration area. Flux densities of the main compact sources present in the field (Supplementary Fig. 4) are also reported in Supplementary Table 3. To produce the spectral-index map shown in Fig. 3, the spectrum of each pixel was fitted with a power law and only pixels above 3σ were included. The errors on the global spectral indices and on the spectral-index map (Supplementary Fig. 5) were obtained using the following formula:

$$\alpha_{\rm err} = \frac{1}{\ln\frac{53}{144}}\sqrt{\left(\frac{\Delta S_{53}}{S_{53}}\right)^2 + \left(\frac{\Delta S_{144}}{S_{144}}\right)^2} \quad (1)$$

where S_{53} and S_{144} are the flux-density (surface brightness) values at the respective frequencies and ΔS_{53} and ΔS_{144} are their corresponding errors. We adopt a Lambda Cold Dark Matter cosmology with matter density $\Omega_{\rm m} = 0.3$, dark energy density $\Omega_\Lambda = 0.7$ and Hubble constant $H_0 = 70\,{\rm km\,s^{-1}\,Mpc^{-1}}$.

SRG/eROSITA observations, data reduction and images. The region where the galaxy group Nest200047 is located was routinely scanned by the SRG observatory (R.S. et al., in preparation), featuring the eROSITA telescope[14], in March and September 2020 and February 2021 for a total of ~645 s over the course of the two half-year all-sky surveys. The eROSITA 0.5–2.3 keV images are shown in Fig. 2 and Supplementary Fig. 3.

In these images, we can clearly see that the diffuse X-ray emission is approximately spherical and centred at the position of MCG+05-10-007, suggesting that the system is in an overall dynamically relaxed state. The X-ray emission in merging systems is indeed expected to show an elongated and/or double-peaked morphology along the merger axis (for example, ref. [22]) and is centred on the brightest central galaxy only in rare cases with peculiar projection effects[46].

We note that the brightest central patch of the X-ray emission (better seen in Fig. 2) is clearly extended in the direction perpendicular to the orientation of the inner radio jets. Similar structures formed by the cool gas have also been found in the cores of giant elliptical galaxies affected by AGN feedback (see, for example, ref. [16] for X-ray imagery of M84).

The proximity of Nest200047 to the Galactic plane (Galactic latitude $b \approx -16°$) has to be considered when interpreting these data. Indeed, the distribution of neutral gas and dust[47–49] suggests (1) variable low-energy photoelectric absorption across the field (Supplementary Fig. 3) and (2) variable contribution from the Galactic diffuse emission. Both factors can affect the appearance of the diffuse emission, especially on scales $\gg$10 arcmin. On scales less than 10–20 arcmin, the

impact of these effects on the 0.5–2.3 keV data is rather modest, but not negligible. This limits the accuracy of the total flux estimates by a factor of ~2.

X-ray surface-brightness profile, luminosity and mass. Using the eROSITA map described above, we derived the radial profile of the X-ray emission as shown in Supplementary Fig. 6. From the plot we can see that the diffuse X-ray emission can be traced up to ~20–30 arcmin from the group centre and that an excess in the central regions is present with respect to a β-model. While deeper observations are required to quantify a possible contribution of the central AGN to this excess, this trend points to the presence of a cool core.

For the spectral analysis we have selected a 13 arcmin circle around the central AGN. Given the complexity of the foreground and low-energy absorption discussed in the 'SRG/eROSITA observations, data reduction and images' section, we have experimented with different regions to estimate and subtract the contribution of the foreground spectra. We have concluded that a 13–29 arcmin annulus is a reasonable choice for the 'background' region. The spectra were fitted with the AtomDB/APEC (Atomic Database for Astrophysics/Astrophysical Plasma Emission Code) thermal plasma emission model (http://atomdb.org; ref. [50]). From the X-ray spectra and the optical observations (Supplementary Section 1) the effective hydrogen-column density was found to be $N_{\rm H} \approx 5 \times 10^{21}$ cm^{-2}. The best-fitting value for the gas temperature is $kT_X \approx 2$ keV. As expected, this value depends on the choice of the background region and lies in the range 1.5–2.5 keV. The 0.5–2 keV X-ray luminosity of the group within a 30 arcmin circle (after correction for Milky Way absorption) is $L_X \approx (5\text{–}10) \times 10^{42}$ erg s^{-1}.

Using the β-model fit to the surface-brightness profile (core radius $r_c \approx 7$ arcmin, corresponding to a physical size of ~140 kpc and $\beta = 0.64$; Supplementary Fig. 6), one can estimate the gas mass of the group. For a gas metallicity varying between 0.3 and 1 times the solar value and for an absorption column density of $\sim 5 \times 10^{21}$ cm^{-2}, the resulting $M_{\rm gas}$ varies from $2 \times 10^{12} M_\odot$ to $5 \times 10^{12} M_\odot$. Assuming the gas mass fraction within R_{500} (the radius within which the average mass density is 500-timesthe critical density of the universe at the redshift of this galaxy group) to be $f_{\rm gas} \approx 0.07$, typical for galaxy groups (for example, ref. [51]), the total mass (M_{500}) of the Nest200047 group is then $3 \times 10^{13} M_\odot$ to $7 \times 10^{13} M_\odot$, about a factor of a few lower than the mass derived from the infrared luminosity of the system (Supplementary Section 1).

Pressure derivation. To investigate the pressure balance between the non-thermal radio-emitting plasma and its surrounding thermal IGrM we used the following approach. For the non-thermal plasma, we made the classical assumption of minimum energy and assumed the magnetic field to be uniformly distributed across the considered volume; moderate deviations from magnetic field or electron uniformity make little difference to these calculations[52]. For the calculation we used the PYSYNCH software (see https://github.com/mhardcastle/pysynch), which provides a Python interface for the code of ref. [53]. We adopted a Jaffe–Perola[54] aged electron spectrum, with a minimum Lorentz factor $\gamma_{\rm min} = 1$ and a low-energy injection energy index $q = 2\alpha + 1 = 2.2$, which matches the observed low-frequency spectral index in the inner jets, marked as A, as well as being in agreement with observations of Fanaroff-Riley I radio galaxies[55,56]. The spectrum was given a radiative age of 250 Myr, assuming a self-consistent loss-field strength of 4 μG and inverse-Compton losses appropriate to the redshift of the source, which gives an approximate fit to the spectral index observed between 53 and 144 MHz for these components (see further spectral ageing analysis below). For true minimum energy, we assume an electron-positron plasma, so that there are no non-radiating particles. Volumes are computed assuming a prolate ellipsoidal geometry ($V = 4/3\pi a^2 b$, where a and b are the ellipsoid semi-axes). We stress, however, that the final pressure values do not significantly depend on the assumed volume (as pressure scales with the volume as $p \propto V^{4/7}$). The final values of volume, magnetic field and pressure are reported in Supplementary Table 4.

We then computed the IGrM thermal pressure using the relation $p_{\rm th} \approx 1.9 n_{\rm e} kT$. If we consider an electron density in the core $n_{\rm e} \approx 0.5 \times 10^{-3}$ cm^{-3} and a temperature in the range $kT = 1.5\text{–}2.5$ keV, as derived from the X-ray data, we get a thermal pressure in the range $p_{\rm th} \approx (2\text{–}4) \times 10^{-12}$ dyn cm^{-2}. At the position of the structures D2 and D3 (approximately 150 kpc from the group centre) we expect that the IGrM pressure should drop by a factor of ~2 to about $p_{\rm th} \approx 10^{-12}$ dyn cm^{-2}.

Overall, the thermal pressure is about an order of magnitude above the non-thermal minimum pressure values shown in Supplementary Table 4, which is similar to the typical ratio of minimum pressure to external thermal pressure seen in FRI radio galaxies[57]. Since the radio structures cannot in reality be under pressured, this implies a non-negligible contribution from non-radiating particles (for example, protons) that dominate the energetics of the large-scale structures. We note, however, that if the plasma is in pressure balance with the external medium, any possible deviation from equipartition would imply a tighter upper limit on the contribution of non-radiating particles.

Timescales and powers. To investigate the age of the non-thermal plasma we estimated the rising time and the radiative age of the two main bubbles C2 and D3.

We computed the rising time using the standard approach $t = H/v$, where v is the bubble velocity and H is its (projected) height from the group centre (for example, ref. [25]). An upper limit to the bubble velocity is provided by the sound speed, which can be approached in case the size of the bubble is comparable with the scale height of the atmosphere. This can be computed as:

$$v_{c_{\rm s}} = \sqrt{\Gamma \frac{kT}{\mu m_{\rm p}}}, \quad (2)$$

where kT is the average IGrM temperature equal to $kT_X \approx 2$ keV as obtained from the X-ray analysis (the 'X-ray surface-brightness profile, luminosity and mass' section), $\mu = 0.62$ is the mean molecular weight, $\Gamma = 5/3$ is the adiabatic index and $m_{\rm p}$ is the proton mass. The derived sound speed is equal to $v_{c_{\rm s}} = 720$ km s^{-1}, implying minimum rising times equal to ~120 Myr for the bubble C2 and ~240 Myr for the bubble D3, if $H_{\rm C2} \approx 90$ kpc and $H_{\rm D3} \approx 170$ kpc are assumed.

A more realistic speed value can be obtained based on buoyancy arguments using the following relation:

$$v_{\rm buoy} = \sqrt{\frac{2gV}{\Phi C}}, \quad (3)$$

where g is the gravitational acceleration, V the volume of the bubble, Φ the cross section ($\Phi_{\rm C2} = \pi a^2$; $\Phi_{\rm D3} = \pi ab$) of the bubble and C the drag coefficient. We assumed $C = 0.75$ (ref. [18]) and $g = (2\sigma^2)/H$ (ref. [58]), where the velocity dispersion is set to $\sigma = 421$ km s^{-1} (Supplementary Section 1). The derived buoyancy speeds are $v_{\rm buoy,C2} \approx 670$ km s^{-1} and $v_{\rm buoy,D3} \approx 500$ km s^{-1}, implying rising times of $t_{\rm buoy,C2} \approx 130$ Myr for the bubble C2 and $t_{\rm buoy,D3} \approx 350$ Myr for the bubble D3. A summary of the bubble properties is presented in Supplementary Table 5. Of course, these age values should be considered as first-order estimates. For example, in the case of non-spherical bubbles, the buoyancy speed is expected to be a factor of a few lower than in the idealized case of a spherical shape[59]. Bubble transport times can further increase in case other processes, such as turbulence and magneto–thermal instabilities, play a role in the system. Overall, the presented buoyancy time estimates can safely be considered as lower limits on the bubble age.

Based on the bubble age estimates presented above, the bubble power is calculated as $P_{\rm bubble} = p_{\rm th} V / t_{\rm buoy}$. Assuming pressure values in the range $p_{\rm th} = (1\text{–}4) \times 10^{-12}$ dyn cm^{-2} (the 'Pressure derivation section') we obtain $P_{\rm bubble,C2} = 3 \times 10^4\text{–}1 \times 10^{42}$ erg s^{-1} and $P_{\rm bubble,D3} = (1\text{–}4) \times 10^{42}$ erg s^{-1}.

Using the observed spectral-index trend shown in Fig. 3, we also derived upper limits to the radiative age of the plasma in the different regions of the source. In particular, we used the Broadband Radio Astronomy Tools (BRATS) software[60], which can model radio spectra by numerically integrating the radiative age equations (including the radiative losses of the plasma through synchrotron emission and inverse-Compton scattering with the cosmic microwave background, CMB). We simulated spectra at many age steps using a Jaffe–Perola model[54] and fixing the magnetic field to the conservative value of $B = 1/\sqrt{(3)} B_{\rm CMB} = 1.95$ μG (which corresponds to the minimum radiative losses allowed for a plasma at a given redshift) and the injection index to the conservative value of $\alpha_{\rm inj} = 0.5$ (the lowest allowed by the Fermi theory). By comparing the spectral index in the frequency range 53–144 MHz for each modelled spectrum (each representing a different age) with the empirical spectral index in the same frequency range shown in Fig. 3, we inferred that it takes a maximum of 200–300 Myr for the plasma to get a spectral index in the range $\alpha_{144\ \rm MHz}^{53\ \rm MHz} = 0.75\text{–}1$ (as observed in D2), 400 Myr to get $\alpha_{144\ \rm MHz}^{53\ \rm MHz} \approx 1.4$ (as observed in D3) and 350 Myr to get $\alpha_{144\ \rm MHz}^{53\ \rm MHz} \approx 1.2$ (as observed in C2). As the aforementioned values are computed assuming minimum values for the magnetic field and injection index they can be considered as upper limits, which can further reduce if adiabatic losses are taken into account. The radiative values can therefore be considered consistent with the dynamical age presented above.

Turbulence and energy flux. If we assume that the curvature observed in the filaments over scales of $L \approx 100$ kpc is originated by the shear-velocity field, and assuming this corresponds to the turbulence injection scale, we can derive that the turbulence velocity at such scales is $\mathrm{d}v_0 = L/t_{\rm buoy} \approx 280$ km s^{-1} (assuming $t_{\rm buoy} = 350$ Myr), which corresponds to a Mach number $M = \mathrm{d}v_0/v_{c_{\rm s}} \approx 0.4$. The turbulence velocity at a scale equal to the filament's height ($l \approx 10$ kpc) is then:

$$\mathrm{d}v(l) = \mathrm{d}v_0 \times (l/L)^{1/3} \approx 130\ \mathrm{km\ s^{-1}} \quad (4)$$

When $\mathrm{d}v(l)$ reaches the Alfven velocity $v_{\rm A}$ the tension produced by the magnetic fields is no longer negligible. In the case of a Kolmogorov cascade, the Alfven scale is $l_{\rm A} = L \times M_{\rm A}^{-3}$, where $M_{\rm A} = \mathrm{d}v_0/v_{\rm A}$ is the Alfven Mach number. The Alfven scale can be then written as:

$$\mathrm{l_A} = 2\ \mathrm{kpc} \times (\mathrm{t}/350\ \mathrm{Myr})^3 \times (\mathrm{L}/100\ \mathrm{kpc})^{-2} \times (\beta_{\rm pl}/100)^{-3/2}. \quad (5)$$

where t is the time, L is the length scale and the plasma beta $\beta_{\rm pl} = p_{\rm th}/p_{\rm nth} = (6/5) \cdot (v_{c_{\rm s}}/v_{\rm A})^2$. Assuming $t = 350$ Myr, $L = 100$ kpc and $\beta_{\rm pl} = 50\text{–}200$ we find that below a scale of 1–5 kpc we enter the MHD regime and magnetic fields can play a role in preventing the filaments from bending.

Finally, the energy flux of the turbulence can be computed by using the following expression:

$$f = 1/2 \times \rho \times \mathrm{d}v_0^3/L \times V. \quad (6)$$

From this and assuming the volume of the bubble D3, a velocity of $\mathrm{d}v_0 = 280\,\mathrm{km\,s^{-1}}$, a density of $\rho = n_e \times m_p$ with $n_e = 0.5 \times 10^{-3}$, and a scale of $L = 100\,\mathrm{kpc}$, we get that the energy flux dissipated by the turbulence into IGrM heat is $f \approx 4 \times 10^{41}\,g\,s^{-3}$.

Data availability

The radio observations are available in the LOFAR long-term archive (https://lta.lofar.eu/) and radio images are available at https://doi.org/10.20371/INAF/DS/2021_00002. The X-ray datasets are not yet publicly available. Their proprietary scientific exploitation rights were granted by the project funding agencies (Roscosmos and DLR) to two consortia led by MPE (Germany) and IKI (Russia), respectively. The SRG–eROSITA all-sky survey data will be released publicly after a minimum period of two years. The exact release date for the data belonging to the consortium led by IKI is yet to be decided. All other data and figures within this paper are available from the corresponding author upon reasonable request.

Code availability

The codes that support the figures within this paper and other findings of this study are available from the corresponding author upon reasonable request.

Received: 16 September 2020; Accepted: 16 August 2021;
Published online: 18 October 2021

References

1. McNamara, B. R. & Nulsen, P. E. J. Heating hot atmospheres with active galactic nuclei. *Ann. Rev. Astron. Astrophys.* **45**, 117–175 (2007).
2. Fabian, A. C. Observational evidence of active galactic nuclei feedback. *Ann. Rev. Astron. Astrophys.* **50**, 455–489 (2012).
3. Gull, S. F. & Northover, K. J. E. Bubble model of extragalactic radio sources. *Nature* **244**, 80–83 (1973).
4. Werner, N., McNamara, B. R., Churazov, E. & Scannapieco, E. Hot atmospheres, cold gas, AGN feedback and the evolution of early type galaxies: a topical perspective. *Space Sci. Rev.* **215**, 5 (2019).
5. Dunn, R. J. H., Fabian, A. C. & Taylor, G. B. Radio bubbles in clusters of galaxies. *Mon. Not. R. Astron. Soc.* **364**, 1343–1353 (2005).
6. Churazov, E., Forman, W., Jones, C. & Böhringer, H. Asymmetric, arc minute scale structures around NGC 1275. *Astron. Astrophys.* **356**, 788–794 (2000).
7. Brüggen, M. Simulations of buoyant bubbles in galaxy clusters. *Astrophys. J.* **592**, 839–845 (2003).
8. Reynolds, C. S., McKernan, B., Fabian, A. C., Stone, J. M. & Vernaleo, J. C. Buoyant radio lobes in a viscous intracluster medium. *Mon. Not. R. Astron. Soc.* **357**, 242–250 (2005).
9. Ruszkowski, M., Enßlin, T. A., Brüggen, M., Begelman, M. C. & Churazov, E. Cosmic ray confinement in fossil cluster bubbles. *Mon. Not. R. Astron. Soc.* **383**, 1359–1365 (2008).
10. Tully, R. B. Galaxy groups: a 2MASS catalog. *Astron. J.* **149**, 171 (2015).
11. Huchra, J. P., Macri, L. M., Masters, K. L., Jarrett, T. H. & Berlind, P. et al. The 2MASS Redshift Survey—description and data release. *Astrophys. J. Suppl.* **199**, 26 (2012).
12. van Haarlem, M. P., Wise, M. W., Gunst, A. W., Heald, G. & McKean, J. P. et al. LOFAR: the Low-Frequency Array. *Astron. Astrophys.* **556**, A2 (2013).
13. Shimwell, T. W., Tasse, C., Hardcastle, M. J., Mechev, A. P. & Williams, W. L. et al. The LOFAR Two-Metre Sky Survey. II. First data release. *Astron. Astrophys.* **622**, A1 (2019).
14. Predehl, P., Andritschke, R., Arefiev, V., Babyshkin, V. & Batanov, O. et al. The eROSITA X-ray telescope on SRG. *Astron. Astrophys.* **647**, A1 (2021).
15. Schoenmakers, A. P., de Bruyn, A. G., Röttgering, H. J. A., van der Laan, H. & Kaiser, C. R. Radio galaxies with a 'double-double morphology' I. Analysis of the radio properties and evidence for interrupted activity in active galactic nuclei. *Mon. Not. R. Astron. Soc.* **315**, 371–380 (2000).
16. Finoguenov, A. & Jones, C. Chandra observation of M84, a radio lobe elliptical galaxy in the Virgo cluster. *Astrophys. J. Lett.* **547**, L107–L110 (2001).
17. Owen, F. N., Eilek, J. A. & Kassim, N. E. M87 at 90 centimeters: a different picture. *Astrophys. J.* **543**, 611–619 (2000).
18. Churazov, E., Brüggen, M., Kaiser, C. R., Böhringer, H. & Forman, W. Evolution of buoyant bubbles in M87. *Astrophys. J.* **554**, 261–273 (2001).
19. Yang, H.-Y. K., Gaspari, M. & Marlow, C. The impact of radio AGN bubble composition on the dynamics and thermal balance of the intracluster medium. *Astrophys. J.* **871**, 6 (2019).
20. Markevitch, M., Govoni, F., Brunetti, G. & Jerius, D. Bow shock and radio halo in the merging cluster A520. *Astrophys. J.* **627**, 733–738 (2005).
21. Enßlin, T. A. & Brüggen, M. On the formation of cluster radio relics. *Mon. Not. R. Astron. Soc.* **331**, 1011–1019 (2002).
22. Rajpurohit, K., Hoeft, M., van Weeren, R. J., Rudnick, L. & Röttgering, H. J. A. et al. Deep VLA observations of the cluster 1RXS J0603.3+4214 in the frequency range of 1–2 GHz. *Astrophys. J.* **852**, 65 (2018).
23. de Gasperin, F., van Weeren, R. J., Brüggen, M., Vazza, F. & Bonafede, A. et al. A new double radio relic in PSZ1 G096.89+24.17 and a radio relic mass–luminosity relation. *Mon. Not. R. Astron. Soc.* **444**, 3130–3138 (2014).
24. Wise, M. W., McNamara, B. R., Nulsen, P. E. J., Houck, J. C. & David, L. P. X-Ray supercavities in the Hydra A cluster and the outburst history of the central galaxy's active nucleus. *Astrophys. J.* **659**, 1153–1158 (2007).
25. Bîrzan, L., Rafferty, D. A. & McNamara, B. R. A systematic study of radio-induced X-ray cavities in clusters, groups, and galaxies. *Astrophys. J.* **607**, 800–809 (2004).
26. O'Neill, S. M., De Young, D. S. & Jones, T. W. Three-dimensional magnetohydrodynamic simulations of buoyant bubbles in galaxy clusters. *Astrophys. J.* **694**, 1317–1330 (2009).
27. Sunyaev, R. A., Norman, M. L. & Bryan, G. L. On the detectability of turbulence and bulk flows in X-ray clusters. *Astron. Lett.* **29**, 783–790 (2003).
28. Porter, D. H., Jones, T. W. & Ryu, D. Vorticity, shocks, and magnetic fields in subsonic, ICM-like turbulence. *Astrophys. J.* **810**, 93 (2015).
29. Xu, S., Ji, S. & Lazarian, A. On the formation of density filaments in the turbulent interstellar medium. *Astrophys. J.* **878**, 157 (2019).
30. Zhuravleva, I., Churazov, E., Schekochihin, A. A., Allen, S. W. & Arévalo, P. et al. Turbulent heating in galaxy clusters brightest in X-rays. *Nature* **515**, 85–87 (2014).
31. Ehlert, K., Weinberger, R., Pfrommer, C., Pakmor, R. & Springel, V. Simulations of the dynamics of magnetized jets and cosmic rays in galaxy clusters. *Mon. Not. R. Astron. Soc.* **481**, 2878–2900 (2018).
32. de Gasperin, F., Dijkema, T. J., Drabent, A., Mevius, M. & Rafferty, D. et al. Systematic effects in LOFAR data: a unified calibration strategy. *Astron. Astrophys.* **622**, A5 (2019).
33. van Weeren, R. J., Williams, W. L., Hardcastle, M. J., Shimwell, T. W. & Rafferty, D. A. et al. LOFAR facet calibration. *Astrophys. J. Suppl.* **223**, 2 (2016).
34. Williams, W. L., van Weeren, R. J., Röttgering, H. J. A., Best, P. & Dijkema, T. J. et al. LOFAR 150-MHz observations of the Boötes Field: catalogue and source counts. *Mon. Not. R. Astron. Soc.* **460**, 2385–2412 (2016).
35. Tasse, C., Shimwell, T., Hardcastle, M. J., O'Sullivan, S. P. & van Weeren, R. et al. The LOFAR Two-Meter Sky Survey: deep fields data release 1. I. Direction-dependent calibration and imaging. *Astron. Astrophys.* **648**, A1 (2021).
36. Tasse, C. Nonlinear Kalman filters for calibration in radio interferometry. *Astron. Astrophys.* **566**, 126 (2014).
37. Smirnov, O. M. & Tasse, C. Radio interferometric gain calibration as a complex optimization problem. *Mon. Not. R. Astron. Soc.* **449**, 2668–2684 (2015).
38. Tasse, C., Hugo, B., Mirmont, M., Smirnov, O. & Atemkeng, M. et al. Faceting for direction-dependent spectral deconvolution. *Astron. Astrophys.* **611**, A87 (2018).
39. van Weeren, R. J., Shimwell, T. W., Botteon, A., Brunetti, G. & Brüggen, M. LOFAR observations of galaxy clusters in HETDEX. Extraction and self-calibration of individual LOFAR targets. *Astron. Astrophys.* **651**, A115 (2021).
40. Offringa, A. R., McKinley, B., Hurley-Walker, N., Briggs, F. H. & Wayth, R. B. et al. WSCLEAN: an implementation of a fast, generic wide-field imager for radio astronomy. *Mon. Not. R. Astron. Soc.* **444**, 606–619 (2014).
41. Offringa, A. R., van de Gronde, J. J. & Roerdink, J. B. T. M. A morphological algorithm for improving radio-frequency interference detection. *Astron. Astrophys.* **539**, A95 (2012).
42. de Gasperin, F., Lazio, T. J. W. & Knapp, M. Radio observations of HD 80606 near planetary periastron. II. LOFAR low band antenna observations at 30–78 MHz. *Astron. Astrophys.* **644**, A157 (2020).
43. Mevius, M., van der Tol, S., Pandey, V. N., Vedantham, H. K. & Brentjens, M. A. et al. Probing ionospheric structures using the LOFAR radio telescope. *Radio Sci.* **51**, 927–941 (2016).
44. de Gasperin, F., Mevius, M., Rafferty, D. A., Intema, H. T. & Fallows, R. A. The effect of the ionosphere on ultra-low-frequency radio-interferometric observations. *Astron. Astrophys.* **615**, A179 (2018).
45. de Gasperin, F., Williams, W. L., Best, P., Brüggen, M. & Brunetti, G. et al. The LOFAR LBA Sky Survey. I. Survey description and preliminary data release. *Astron. Astrophys.* **648**, A104 (2021).
46. Rossetti, M., Gastaldello, F., Ferioli, G., Bersanelli, M. & De Grandi, S. et al. Measuring the dynamical state of Planck SZ-selected clusters: X-ray peak-BCG offset. *Mon. Not. R. Astron. Soc.* **457**, 4515–4524 (2016).
47. HI4PI Collaboration, Ben Bekhti, N., Flöer, L., Keller, R. & Kerp, J. et al. HI4PI: a full-sky H I survey based on EBHIS and GASS. *Astron. Astrophys.* **594**, A116 (2016).

48. Planck Collaboration, Abergel, A., Ade, P. A. R., Aghanim, N., Alves, M. I. R. & Aniano, G. et al. Planck 2013 results. XI. All-sky model of thermal dust emission. *Astron. Astrophys.* **571**, A11 (2014).
49. Schlegel, D. J., Finkbeiner, D. P. & Davis, M. Maps of dust infrared emission for use in estimation of reddening and cosmic microwave background radiation foregrounds. *Astrophys. J.* **500**, 525–553 (1998).
50. Foster, A. R., Ji, L., Smith, R. K. & Brickhouse, N. S. Updated atomic data and calculations for X-ray spectroscopy. *Astrophys. J.* **756**, 128 (2012).
51. Lovisari, L., Reiprich, T. H. & Schellenberger, G. Scaling properties of a complete X-ray selected galaxy group sample. *Astron. Astrophys.* **573**, A118 (2015).
52. Hardcastle, M. J. Synchrotron and inverse-Compton emission from radio galaxies with non-uniform magnetic field and electron distributions. *Mon. Not. R. Astron. Soc.* **433**, 3364–3372 (2013).
53. Hardcastle, M. J., Birkinshaw, M. & Worrall, D. M. Magnetic field strengths in the hotspots of 3C 33 and 111. *Mon. Not. R. Astron. Soc.* **294**, 615–621 (1998).
54. Jaffe, W. J. & Perola, G. C. Dynamical models of tailed radio sources in clusters of galaxies. *Astron. Astrophys.* **26**, 423–435 (1973).
55. Fanaroff, B. L. & Riley, J. M. The morphology of extragalactic radio sources of high and low luminosity. *Mon. Not. R. Astron. Soc.* **167**, 36 (1974).
56. Carilli, C. L., Perley, R. A., Dreher, J. W. & Leahy, J. P. Multifrequency radio observations of Cygnus A: spectral aging in powerful radio galaxies. *Astrophys. J.* **798**, 88 (2015).
57. Croston, J. H., Ineson, J. & Hardcastle, M. J. Particle content, radio-galaxy morphology, and jet power: all radio-loud AGN are not equal. *Mon. Not. R. Astron. Soc.* **476**, 1614–1623 (2018).
58. Binney, J., Tremaine, S. *Galactic Dynamics. Princeton Univ. Press* (1987).
59. Zhang, C., Churazov, E. & Schekochihin, A. A. Generation of internal waves by buoyant bubbles in galaxy clusters and heating of intracluster medium. *Mon. Not. R. Astron. Soc.* **478**, 4785–4798 (2018).
60. Harwood, J. J., Hardcastle, M. J., Croston, J. H. & Goodger, J. L. Spectral ageing in the lobes of FR-II radio galaxies: new methods of analysis for broad-band radio data. *Mon. Not. R. Astron. Soc.* **435**, 3353–3375 (2013).

Acknowledgements

M. Brienza sincerely thanks F. Santoro, K. Rajpurohit and F. Vazza for their help and very useful discussions. M. Brienza and A. Bonafede acknowledge support from the European Research Council (ERC-Stg) DRANOEL (Deciphering Radio Non-thermal Emission), no 714245. M. Brienza acknowledges support by the ERC-Stg project MAGCOW (The Magnetised Cosmic Web), no 714196. A. Bonafede acknowledges support from the MIUR (Ministero dell'Istruzione dell'Università e della Ricerca) grant FARE (Framework per l'Attrazione e il Rafforzamento Delle Eccellenze) "SMS". R.J.v.W. acknowledges support from the ERC Starting Grant ClusterWeb 804208. A. Botteon acknowledges support from the VIDI research programme with project number 639.042.729, which is financed by the Netherlands Organisation for Scientific Research (NWO). A.S. is supported by the Women In Science Excel programme of the NWO and acknowledges the World Premier Research Center Initiative and the Kavli Institute for the Physics and Mathematics of the Universe (Kavli IPMU) for the continued hospitality. The Netherlands Institute for Space Research (SRON) is supported financially by NWO. M. Brüggen acknowledges support from the Deutsche Forschungsgemeinschaft under Germany's Excellence Strategy (EXC 2121 "Quantum Universe") 390833306. S.J.D.P. would like to acknowledge support from the European Research Council advanced grant H2020-ERC-2016-ADG-74302 under the European Union's Horizon 2020 Research and Innovation programme. F.G. and G.B. acknowledge support from INAF mainstream project 'Galaxy Clusters Science with LOFAR' 1.05.01.86.05. I.B., R.B. and R.S. thank TUBITAK (Scientific and Technological Research Council of Turkey), IKI, KFU (Kazan Federal University) and AST for partial support in using RTT150 (the Russian–Turkish 1.5 m telescope in Antalya). The work of I.B. was funded by the grant 671-2020-0052 to Kazan Federal University. LOFAR, designed and constructed by ASTRON, has facilities in several countries, which are owned by various parties (each with their own funding sources), and are collectively operated by the International LOFAR Telescope Foundation under a joint scientific policy. The International LOFAR Telescope Foundation resources have benefited from the following recent major funding sources: CNRS-INSU (Institut National des Sciences de l'Univers), Observatoire de Paris and Université d'Orléans, France; BMBF (Federal Ministry of Education and Research), MIWF-NRW (Ministeriums für Kultur und Wissenschaft in Nordrhein-Westfalen) and MPG (Max Planck Society), Germany; Science Foundation Ireland, Department of Business, Enterprise and Innovation, Ireland; NWO, the Netherlands; the Science and Technology Facilities Council, United Kingdom; Ministry of Science and Higher Education, Poland and The Istituto Nazionale di Astrofisica (INAF), Italy. Part of this work was carried out on the Dutch national e-infrastructure with the support of the SURF Cooperative through grant e-infra 160022 and 160152. The LOFAR software and dedicated reduction packages on https://github.com/apmechev/GRID_LRT were deployed on the e-infrastructure by the LOFAR e-infragroup, consisting of J.B.R. Oonk (ASTRON and Leiden Observatory), A.P. Mechev (Leiden Observatory) and T. Shimwell (ASTRON) with support from N. Danezi (SURFsara) and C. Schrijvers (SURFsara). The Jülich LOFAR Long Term Archive and the German LOFAR network are both coordinated and operated by the Jülich Supercomputing Centre and computing resources on the supercomputer JUWELS at the Jülich Supercomputing Centre were provided by the Gauss Centre for supercomputing e.V (Eingetragener Verein). (grant CHTB00) through the John von Neumann Institute for Computing. This research made use of the University of Hertfordshire high-performance computing facility and the LOFAR UK computing facility located at the University of Hertfordshire and supported by the Science and Technology Facilities Council (STFC) (ST/P000096/1), and of the Italian LOFAR IT computing infrastructure supported and operated by INAF, and by the Physics Department of Turin University (under an agreement with Consorzio Interuniversitario per la Fisica Spaziale) at the C3S Supercomputing Centre, Italy. This work is based on observations with the eROSITA telescope onboard the SRG space observatory. The SRG observatory was built by Roskosmos in the interests of the Russian Academy of Sciences represented by IKI in the framework of the Russian Federal Space Program, with the participation of the Deutsches Zentrum für Luft- und Raumfahrt (DLR). The eROSITA X-ray telescope was built by a consortium of German Institutes led by the Max Planck Institute for Extraterrestrial Physics (MPE), and supported by DLR. The SRG spacecraft was designed, built, launched and is operated by the Lavochkin Association and its subcontractors. The science data are downlinked via the Deep Space Network Antennae in Bear Lakes, Ussurijsk and Baikonur, funded by Roskosmos. The eROSITA data used in this work were converted to calibrated event lists using the eSASS software system developed by the German eROSITA Consortium and analysed using proprietary data reduction software developed by the Russian eROSITA Consortium. This research made use of APLpy, an open-source plotting package for Python hosted at: http://aplpy.github.com.

Author contributions

M. Brienza coordinated the research, performed the radio imaging and radio analysis and wrote the manuscript. T.W.S coordinated the LOFAR HBA data processing and helped coordinate the project. F.d.G. led the LOFAR LBA observing proposal and performed the data reduction. A. Bonafede helped with the analysis of the radio data and with coordination of the project. A. Botteon helped with the LOFAR HBA data processing and with manuscript revision. M. Brüggen and G.B. helped with interpretation of the source and with manuscript revision. A.C. contributed to the system identification and the analysis of the optical properties of the system. M.J.H. helped with the LOFAR HBA data processing, with interpretation of the source and with manuscript revision. E.C., I.K. and N.L. analyzed the SRG/eROSITA data and contributed to interpretation of the results and writing the manuscript. I.B. performed the optical observations and analysis of the source and contributed to the interpretation of the results and writing the manuscript. R.B. and R.S. contributed to the interpretation of the results and writing the manuscript. R.J.v.W. helped with the LOFAR HBA data processing and with manuscript revision. F.G. helped with the interpretation of the results and manuscript revision. S.M. and A.S. helped revise the manuscript. C.T.helped with the LOFAR HBA data processing. S.P. led the LOFAR HBA observing proposal.

Competing interests

The authors declare no competing interests.

Additional information

Supplementary information The online version contains supplementary material available at https://doi.org/10.1038/s41550-021-01491-0.

Correspondence and requests for materials should be addressed to M. Brienza.

Peer review information *Nature Astronomy* thanks the anonymous reviewers for their contribution to the peer review of this work.

Reprints and permissions information is available at www.nature.com/reprints.

Publisher's note Springer Nature remains neutral with regard to jurisdictional claims in published maps and institutional affiliations.